Manuscript prepared for J. Name
with version 5.0 of the LaTeX class copernicus.cls.
Date: 26 May 2014

Dynamics of turbulent western boundary currents at low latitude in a shallow water model

C.Q.C. AKUETEVI[1, 2, 3] and A. WIRTH[2]

[1]Université de Grenoble, France
[2]Laboratoire des Ecoulements Géophysiques et Industriels, CNRS UMR 5519, Grenoble
[3]Laboratoire de Glaciologie et Géophysique de l'Environnement, CNRS UMR 5183, Grenoble

Correspondence to: C.Q.C. AKUETEVI
(Cyrille.Akuetevi@legi.grenoble-inp.fr)

Abstract. The dynamics of low latitude turbulent western boundary currents, subject to two different types of idealized wind forcing, Monsoon Wind and Trade Wind, is considered using numerical results from integrations of a reduced gravity shallow-water model. For viscosity values of $1000\text{m}^2\text{s}^{-1}$and above, the boundary layer dynamics compares well to the analytical solutions of the Munk-layer and the inertial-layer, derived from quasigeostrophic theory. Modifications due to variations in the layer thickness (vortex stretching) are only important close to the boundary. When the viscosity is reduced the boundary layer becomes turbulent and coherent structures in form of anticyclonic eddies, bursts (violent detachments of the viscous sub-layer) and dipoles appear. Three distinct boundary layers emerge, the viscous sub-layer, the advective boundary layer and the extended boundary layer. The first is characterized by a dominant vorticity balance between the viscous transport and the advective transport of vorticity. The second by a balance between the advection of planetary vorticity and the advective transport of relative vorticity. The extended boundary layer is the area to which turbulent motion from the boundary extends. The scaling of the three boundary layer thicknesses with viscosity is evaluated.

A pragmatic approach to determine the eddy viscosity diagnostically for coarse resolution numerical models is proposed.

1 Introduction

Strong western boundary currents (WBCs) are a dominant feature of the world's oceans. They are also present at low latitudes in the Atlantic and the Indian oceans, where they are called the North Brazil Current (NBC) and the Somali Current (SC), respectively. We refer the reader to Richardson et al. (1994); Garzoli et al. (2003); Fratantoni and Richardson (2006) for a detailed discussion of the NBC and the subtropical gyre in Atlantic Ocean. A detailed description of the circulation of the northern Indian Ocean, of which the SC is the most energetic part, is given by Schott and McCreary (2001); Schott et al. (2009); Beal and Donohue (2013); Beal et al. (2013). These currents are variable in time. Part of this time dependence is due to the time-dependent forcing and the other part is due to the internal dynamics. In the present study we completely neglect the former by using time-independent forcing. The latter is the subject of the present publication. Even when subject to time-independent forcing, low latitude western boundary currents retroflect (i.e., separated away from the boundary and turn anticyclonically for more than 90^o) and form anticyclonic eddies. The NBC retroflects near 6^o-8^oN and sheds eddies exceeding 450km in overall diameter (see e.g. Richardson et al. (1994); Garzoli et al. (2003); Fratantoni and Richardson (2006)). While the SC and the East African Coastal Current retroflect to form eddies called the Great Whirl (GW) between 5^o-10^oN and the Southern Gyre (SG) near the equator with overall diameter between 350-540km (see e.g. Schott and McCreary (2001); Beal and Donohue (2013); Beal et al. (2013)). There are substantial differences between the Atlantic and the Indian Ocean. One is the forcing by the wind stress field. In the equatorial Atlantic the Trade Winds are the major force. Whereas in the Indian Ocean the seasonally reversing Monsoon Winds dominate. Another difference is the latitudinal inclination of the coast line, it is westward in the Atlantic Ocean and eastward in the Indian Ocean. The important influence of the inclination of the coast line will not be addressed here.

There is a large number of numerical work on the dynamics of the Somali current and the north Brazil current with a realistic coast line and topography (see $i.e.$ Fratantoni et al. (1995); Barnier et al. (2001); Wirth et al. (2002); Garraffo et al. (2003)). Although realistic models permit to represent the observed features of the world's oceans, it is difficult to learn about isolated processes because all the phenomena take part simultaneously in the dynamics and interact non-linearly. The only way to guarantee our understanding of the ocean dynamics is to decompose it into processes.

In the same spirit several idealized numerical studies with a slanted western boundary noted the crucial importance of the slanted boundary in gyre generation (see $i.e.$ Cox (1979); McCreary and Kundu (1988)).

Idealized rectangular basin studies which address the dynamics formation of the large anticyclones were performed (see $i.e.$ Cox (1979); Lin and Hurlburt (1981); Philander and Pacanowski (1981); Philander and Delecluse (1983); McCreary and Kundu (1988)).

A detailed determination of the vorticity balances, fluxes and stability of idealized low latitude turbulent WBCs have been performed by Edwards and Pedlosky (1998a), Edwards and Pedlosky (1998b) on the dssp WBC and by Fox-Kemper (2005) on the dynamics of single and multiple gyres in a barotropic constant depth β-plane model.

All the above works proved with no doubt that the large anticyclones and their non-stationary dynamics have a crucial impact on the mean circulation in the boundary regions. All these studies focused on the larger scale features of the WBCs such as the large anticyclones.

It has been shown in engineering fluid dynamics that boundary-layer dynamics involves different types of coherent structures (see $i.e.$ Aubry et al. (1988); Robinson (1991)). In satellite observations of the SC, small flanking cyclones correlated with the large anticyclone tend to circulate clockwise around it (Beal and Donohue (2013)). The coarse resolution in space and time of satellite data does not allow for a detailed study of these small scale structures. Such flanking vortices are also present in the laboratory experiments of geophysical fluid dynamics (see $i.e.$ Van Heijst and Flor (1989)). these structures are also clearly visible in fine resolution realistic simulations of the ocean dynamics.

The purpose of the present work is the identification and the study of the smaller scale coherent structures, their interaction and their influence on the large-scale circulation. Indeed to the best of our knowledge there is so far no description or theory of near coastal turbulence in the western boundary current, that goes beyond the large anticyclonic eddies. For oceanic WBCs in general, the quantitative description is mainly based on stationary geostrophic Munk-layer theory (Munk (1950)) or inertial-layer theory (Stommel (1995); Fofonoff (1954); Charney (1955)) and the analysis of their stability (see *e.g.* Edwards and Pedlosky (1998b), Ierly and Young (1991)). This is in stark contrast to engineering fluid dynamics, where the turbulent boundary-layer theory is the leading domain since its birth in the beginning of the 20th century (Prandtl (1904)). In this article we study the dynamics of low latitude turbulent WBCs in the viewpoint of boundary-layer theory with emphasis on coherent structures.

In the present work we focus on the dynamics of low latitude turbulent WBCs in a highly idealized configuration, to determine its structure, its dependence on the Reynolds number, by varying the viscosity between experiments, and its response to two distinct wind forcings. Idealized Trade Winds and idealized Monsoon Winds are considered. The experimental set-up comprises essential prerequisites such as a fine resolution throughout the domain and long-time integrations to obtain statistically converged results.

The physical situation considered, the mathematical model to study its dynamics and its numerical implementation are discussed in the next section. Results on the taxonomy of the coherent structures, the turbulent fluxes, their parameterization and the vorticity balance are given in section 4 and discussed in section 5.

2 The Model

2.1 The physical problem considered

To consider the dynamics of low latitude turbulent boundary currents, with an emphasis on the Atlantic and the Indian Oceans, we constructed a highly idealized version of them.

The basin is a rectangular box that straddles the equator with dimensions $L_x \times L_y$ (zonal width and meridional width respectively, values are listed in Table 1). It spans from 1000km south of the

parameter	Value
β, rate of change of Coriolis parameter	2×10^{-11}m^{-1}s^{-1}
τ_0, wind-stress amplitude	0.35/0.4 Nm^{-2}
ν, eddy viscosity coefficient	1000 m^{2}s^{-1}
H, upper-layer thickness	200 m
ρ, upper-layer density	1000 Kgm^{-3}
L_x, east-west extend	6000 km
L_y, north-south extend	4000 km
$g\prime$, reduced gravity	0.03 ms^{-2}

Table 1. *Model parameters*

equator to 3000km north. The domain extends further northward than southward, as our research is directed towards studying the Somali and North Brazil currents, ranging within the most energetic structures in the world's ocean and both occurring north of the equator. The model is comparable to those used in idealized configuration to study mid-latitude gyres (see e.g Jiang et al. (1995); Sushama et al. (2007); Speich et al. (1995)) and low latitude WBCs (see e.g Edwards and Pedlosky (1998a,b); Fox-Kemper (2005)). The Coriolis parameter varies linearly with latitude, this geometry is usually referred to as the equatorial β-plane. We further suppose that the dynamics considered is this of an homogeneous fluid layer of an average thickness of H which superposes a constant density motionless fluid layer of infinite depth. The density difference between the layers is expressed by the reduced gravity g'. These numbers are inspired by the water-mass properties in the Indian Ocean. The layer is forced by a wind shear at its surface. Two types of wind shears are considered, an equatorial easterly Trade Wind (TW) and a Monsoon Wind (MW) which is southerly along the western boundary.

2.2 The mathematical model

The governing reduced-gravity shallow water equations are:

$$\partial_t u + u\partial_x u + v\partial_y u - fv + g'\partial_x\eta = \nu\nabla^2 u + \frac{\tau_x}{\rho(H+\eta)}, \quad (1)$$

$$\partial_t v + u\partial_x v + v\partial_y v + fu + g'\partial_y\eta = \nu\nabla^2 v + \frac{\tau_y}{\rho(H+\eta)}, \quad (2)$$

$$\partial_t\eta + \partial_x[(H+\eta)u] + \partial_y[(H+\eta)v] = 0; \quad (3)$$

here u and v represent the zonal and meridional velocities, respectively and η is the variation of the layer-thickness. The Coriolis parameter is given by

$$f = \beta y, \quad (4)$$

$$g' = \frac{\Delta\rho}{\rho}\cdot g \quad (5)$$

is the reduced gravity, and g the acceleration of gravity. The parameters for the experiments performed here are listed in Table 1. The system is subject to a zonal and meridional wind-stress forcing τ_x, τ_y and no-slip boundary conditions. A Laplacian lateral diffusion with a viscosity ν is used. It is necessary to insure the no-slip lateral boundary condition and its role is also to prevent the accumulation of energy/enstrophy at the smallest scales that are resolved numerically. Please see Frisch et al. (2008), for a detailed discussion of this bottleneck phenomena.

The associated equation for vorticity is:

$$\partial_t \xi + u\partial_x \xi + v\partial_y \xi + \beta v + (\xi + f)(\partial_x u + \partial_y v) - \nu \nabla^2 \xi = F, \tag{6}$$

or in conservative form:

$$\partial_t \xi + \partial_x [u(\xi + f)] + \partial_y [v(\xi + f)] - \nu \nabla^2 \xi = F, \tag{7}$$

where F is the curl of the forcing.

2.3 The wind-stress forcing

As in McCreary and Kundu (1988), the model ocean is forced by wind fields that are composed of patches of the form

$$\tau = \tau_o X(x) Y(y) s(t). \tag{8}$$

Values of the wind strength τ_o are specified below for each type of wind forcing. The offshore and the alongshore structures, $X(x)$ and $Y(y)$, are also described.

The wind-stress implemented in Eqs.(1) and (2) is discriminated into Monsoon Winds forcing

$$(MW) \begin{cases} \tau_x = 0, \\ \tau_y = 0.35 \cdot [\exp(-4(\frac{x}{L_x})^2 - 0.2)][1 - \exp(\frac{-t}{t_c})]. \end{cases} \tag{9}$$

and Trade Winds forcing

$$(TW) \begin{cases} \tau_x = 0.4 \cdot [1 - \exp(\frac{x}{L_x})][\exp(-4(\frac{y}{L_y})^2)][1 - \exp(\frac{-t}{t_c})], \\ \tau_y = 0 \end{cases} \tag{10}$$

In the Atlantic the Trade Winds decay towards the east. In our calculations the decay towards the east also prevents the vanishing of the surface layer. The values of the wind strength τ_o are chosen, so that the transport in the boundary currents are similar at $y = +1500$km for the TW and the MW forcing, for a viscosity $\nu = 1000\mathrm{m}^2\mathrm{s}^{-1}$.

The spin-up time for the wind forcing is $t_c = 180$days.

2.4 The numerical implementation

The numerical method used to solve the Eqs.(1)–(3) is a centered, second-order finite difference scheme in space, using an Arakawa A-grid, and a second order Runge-Kutta scheme is used for time stepping. A fine numerical resolution of square geometry ($\Delta x = \Delta y = 2.5km$) is employed throughout the entire domain. The scheme was successfully tested changing resolution in space and time in Wirth (2013). This uncommon choice, of not using grid refinement at the boundary, is justified by the results presented in section 4, where it is clearly seen that for high Reynolds number flow, parts of the viscous sub-layer are torn of the wall and transported away from it by the surrounding turbulent flow. This leads to small scale structures also far from the boundary. Such kind of process can only be represented when there is fine resolution in both horizontal directions throughout the extended boundary layer (to be defined in subsection 4.4). Please note that the resolution is well below the Munk scale $\delta_M = (\nu/\beta)^{1/3}$, which is around 18km in the lowest viscosity experiment. We favor fine-resolution rather than high-order schemes. The time-step is 90s, which is almost five times shorter than the CFL time-step imposed by the speed of the flow and the gravity waves. In the nonlinear boundary layer the high vorticity in the boundary layer (viscous sub-layer, detailed in 4.6) is intermittently torn of the boundary. This process is the equivalent of bursts in 3D boundary layers (see *e.g.* Robinson (1991)). It is this intermittent, rapid and violent process and its nonlinear evolution that asks for a short time-step. The physical parameters are such that in the present dynamics a vanishing of the fluid layer (outcrop) does not occur.

3 Experiments

The system's behavior is mainly determined by the wind strength τ_o and ν, the two parameters that control the strength of external wind forcing and the lateral viscosity, respectively. Since the two types of wind are set, the spatiotemporal complexity of the system's behavior increases with decreasing ν. The other model parameters are kept constant and are given in Table 1. For both types of wind forcing (TW and MW) experiments for different values of the viscosity were performed. Experiments are referred to by the forcing followed by the viscosity value: MW1000 is an experiment with MW forcing and a viscosity $\nu = 1000\text{m}^2\text{s}^{-1}$. The highest viscosity experiments with $\nu = 1000\text{m}^2\text{s}^{-1}$ converged towards a stationary dynamics, the corresponding Reynolds number based on the maximal average meridional velocity in the boundary current and the Munk-layer thickness at $y = +1500$km is $Re = v_0\delta_M/\nu = 31$ and 42 for TW1000 and MW1000, respectively. The transport in the boundary layer is, to leading order, imposed by the wind forcing over the entire basin, which does not vary within the Monsoon Winds and Trade Winds cases. This leads to the fact, that velocity times the boundary layer thickness is constant and the Reynolds number scales as the inverse of the viscosity. The numerical resolution and scheme allowed to perform calculations with viscosities down to $\nu = 125\text{m}^2\text{s}^{-1}$ for the TW forcing. For the MW forcing the lowest viscosity was $\nu = 300\text{m}^2\text{s}^{-1}$. The reason for the more stable TW experiments lies in the existence of inertial effects that play a stabilizing role, as discussed in subsection 4.4.

In the high viscosity experiments the boundary layer dynamics converges towards a stationary state in about 3000 days of the dynamics. Lower viscosity experiments converge to a statistically stationary state. To increase the significance of the statistics, experiments were performed for 5000 days of the dynamics and averages used herein were calculated over the last 2000 days.

4 Results

4.1 Large-scale Circulation (Validation)

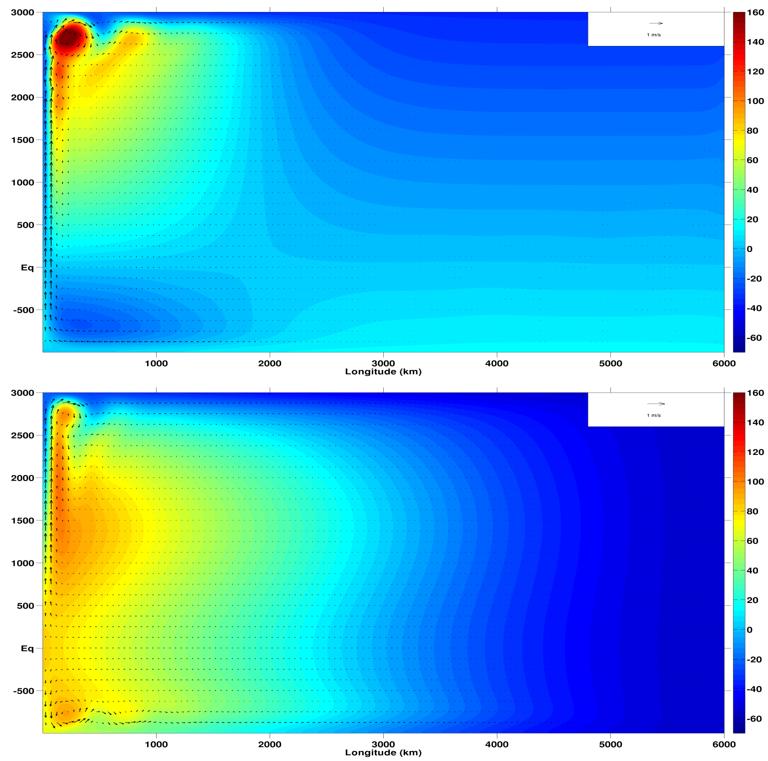

Fig. 1. Instantaneous velocity arrows superimposed on layer thickness variation (η) at time t = 2000days for the high viscosity experiments MW1000 (above) and TW1000 (below). The dynamics converges towards a stationary state before 2000days of the integration and seems to be indistinguishable to the averages over 3000-5000days.

Before proceeding to the more complicated non-linear solutions, it is useful to review the familiar, linear solution which can be determined from a combination of *Sverdrup theory* [Sverdrup (1947)] and *Stommel theory* [Stommel (1948)] with a *Munk-layer theory* [Munk (1950)] and *inertial-layer theory* [Charney (1955)]. It provides a useful baseline to compare the more complicated non-linear flows for the two sets of experiments. Shown in Fig. 1a and Fig. 1b are layer thickness variation (η) contours and horizontal velocity arrows from the laminar experiments MW1000 and TW1000, after the spin-up time, at t = 2000days. Velocity vectors are plotted every 20 x 50 grid points in the x

and y directions. These figures show the classic Sverdrup interior solution with a Munk or inertial boundary-layer (discussed in detail in the next section). The velocity vectors are small in regions where the flow is weak and difficult to distinguish in the figures. In these regions, the sense of the geostrophic flow can be inferred from the η-field.

For both types of wind forcing TW and MW strong western boundary currents with a recirculation in the rest of the domain were observed, as can be seen in Fig 1. With the TW forcing the boundary current is poleward in both hemispheres. The southward boundary current is less strong due to the domain extending only 1000km to the south but 3000km to the north. The MW forcing led to a single gyre extending over the entire domain with the western boundary current crossing the equator in the northward direction. Another important difference between the circulation resulting from MW and TW forcing, is that for the former the boundary current is in the northern direction and the zonal velocity vanishes almost completely except near the southern and northern boundaries of the domain. While in the latter the zonal velocity is westward at low latitudes up to about $y = +1300$km and eastward above (see Fig.2). We will see in the sequel that these relatively small zonal velocities have an important impact on the stability and nature of the boundary current system. For the largest viscosity values, the dynamics converge towards a stationary flow for both types of wind forcing. In experiments with lower viscosities, time dependence arises in the form of coherent anticyclones moving northward along the western boundary. For the lowest viscosity experiments the dynamics are fully turbulent, with chaotic motion over a range of spacial scales (see subsection 4.4). The time averaged large-scale circulation of the low viscosity experiments is qualitatively similar to the stationary flow at high viscosity.

4.2 Laminar Boundary Layers

For the high values of the viscosity the stationary solutions of the boundary layer are, to leading order, given by a balance of the meridional transport of planetary vorticity (4th term in Eq.(6)) and the viscous dissipation (last term on the l.h.s. of Eq.(6)). This dynamic is described by the Munk-layer theory (Munk (1950), Pedlosky (1990)) and the solutions are:

$$v_{\mathrm{M}}(x) = v_{\mathrm{M}}^{0} \exp\left(-\frac{x}{2\delta_{\mathrm{M}}}\right) \sin\left(\frac{\sqrt{3}}{2}\frac{x}{\delta_{\mathrm{M}}}\right) \tag{11}$$

where $\delta_{\mathrm{M}} = (\nu/\beta)^{1/3}$ is the characteristic boundary layer thickness of the Munk-layer and v_{M}^{0} is a velocity scale. There is a fair agreement between Munk-layer theory and our numerical results for the MW and the TW forcing at higher latitude, where inertial effects vanish, as can be seen in Fig.2. Munk-layer theory solution is in geostrophic balance away from the WBC. The solution is obtained by assuming a vorticity balance between the advection of planetary vorticity and lateral viscous dissipation and neglects variations in the layer thickness which are important in our reduced-gravity model (see section 4.6) at low latitude. The vortex stretching is given by the fifth term in Eq.(6). We found the vortex stretching to be important very close to the boundary but decreases rapidly before

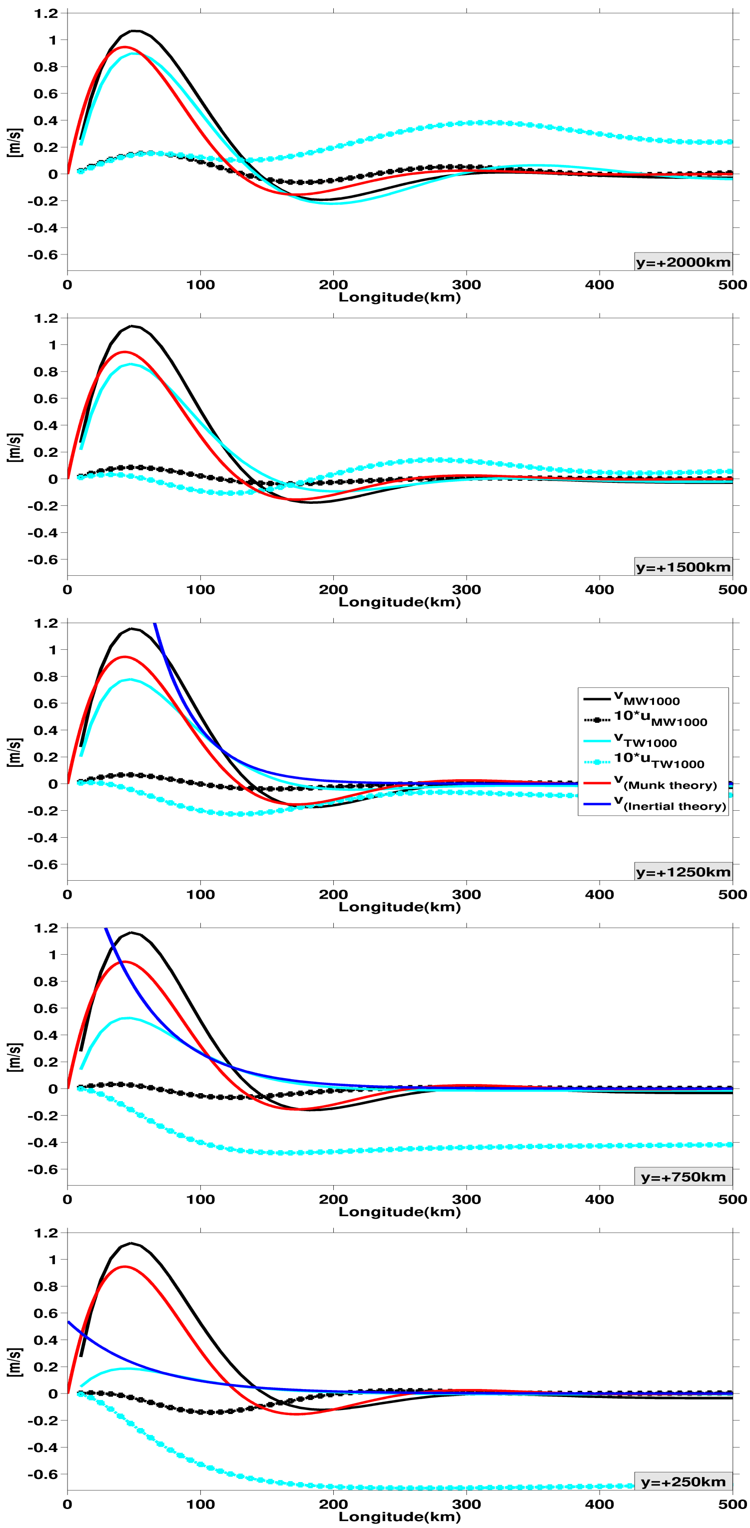

Fig. 2. Zonal profiles of the u and v components for the experiments MW1000 and TW1000 at five latitudes, $y = +2000$, $y = +1500$, $y = +1250$, $y = +750$ and $y = +250$km from top to bottom. Superposed are the zonal profiles of the analytic solutions of Munk-layer theory (red full line) and the analytic solution of inertial-layer theory (red dashed line). The amplitudes v^0_{M} in Eq.(11) and v^0_{I} in Eq.(12) are chosen to best fit the data.

the meridional velocity reaches its maximum (not shown), but does not lead to substantial deviations from the Munk-layer and inertial-layer solutions as can be verified in Fig.2. This is in agreement with the results of Edwards and Pedlosky (1998a). At low latitudes in the TW circulation there is a significant westward velocity. This alters completely the boundary layer structure as the vorticity balance in the outer part of the boundary layer is now between the meridional transport of planetary vorticity (4th term in Eq.(6)) and the westward transport of relative vorticity (second term in Eq.(6)) , leading to an inertial boundary layer (Charney (1955), see also Pedlosky (1990) and Vallis (2006)). The outer part of the boundary layer is now much better fitted (see Fig.2) by the inertial boundary layer solution:

$$v_{\mathrm{I}}(x) = v_{\mathrm{I}}^0 \exp\left(-\frac{x}{\delta_{\mathrm{I}}}\right), \tag{12}$$

where $\delta_{\mathrm{I}} = \sqrt{-u_{\mathrm{I}}(y)/\beta}$ is the characteristic boundary layer thickness of the inertial layer and v_{I}^0 is a velocity scale. u_{I}(y) is the westward zonal velocity just outside the boundary layer, responsible for the inertial effect (see Pedlosky (1979, Sect. 5.6)). At the boundary the inertial solution is modified by viscous dissipation, which is necessary to satisfy the no-slip boundary condition. Such viscous dissipation is also necessary for the basin wide vorticity balance as discussed in subsection 4.6. Note, that the inertial scale δ_{I}, also called the Charney scale, is a result of the large-scale dynamics due to the wind forcing. It depends only weakly on the viscosity. Whereas, the Munk-layer scale δ_{M} depends only on external parameters, it can be calculated independently of the circulation. When $\delta_{\mathrm{I}} > \delta_{\mathrm{M}}$ inertial effects govern the outer part of the boundary layer, prevent it from becoming thinner and stabilize it (see also Ierly and Young (1991)). This explains the increased stability of the equatorward part of the boundary layer in the TW circulation. Please note, that an eastward velocity has no such stabilizing effect. Indeed in the TW experiment there is a eastward average velocity in the northern part of the domain, the Charney scale becomes complex valued and a tendency to spatial and temporal oscillations are observed (see subsection 4.6).

4.3 Coherent structures

4.3.1 Anticyclones

The most conspicuous coherent structures are the anticyclonic eddies along the western boundary. In the MW experiments they start to appear at viscosity values of $\nu = 1000\mathrm{m}^2\mathrm{s}^{-1}$ during the spin-up as poleward travelling waves in the boundary layer. They travel northward along the boundary at a speed of $V_{eddy} \approx 2.3 \cdot 10^{-1}\mathrm{ms}^{-1}$. This speed is faster than the fastest Rossby wave meaning that they do not radiate Rossby waves (Ierly and Young (1991)). Their size increases with a decreasing viscosity. At viscosities of $\nu \approx 500\mathrm{m}^2\mathrm{s}^{-1}$, they are coherent regular vortices. Their diameter is then around the equatorial Rossby radius of deformation $L_\beta = \sqrt{\sqrt{g'H}/\beta} = 350$km, a size that compares well to the size of the eddies in the Somali current (Schott and McCreary (2001), Wirth et al. (2001)) and to the eddies of the North Brazil current (Richardson and Schmitz (1993)). When inspecting the potential vorticity (PV) they appear as negative PV anomalies that move poleward with an average speed of $V_{eddy} \approx 1 \cdot 10^{-1}\text{ms}^{-1}$, while the fluid velocity in their interior reaches a speed of $v_{eddy} = 2\text{ms}^{-1}$. This demonstrates, that the eddies are advected water masses and not wave-like phenomena. A closer inspection of the velocity field shows that they are eddies in almost perfect solid-body rotation and not vortex rings (not shown), with an almost motionless core (eye). One has to mention that in the literature eddy or ring are often used interchangeably to denote the same object. With decreasing viscosity their shape and poleward displacement exhibit a random-like behavior (Wirth et al. (2001)) as can be verified analyzing Hovmöller diagrams (not shown) indicating a chaotic dynamics. For the lower viscosity values the eddy dynamics becomes more chaotic, some of the eddies migrate into the interior of the basin, merge with other eddies or are disintegrated by them in a 2D turbulent eddy dynamics. At the lowest viscosity value of $\nu = 300\text{m}^2\text{s}^{-1}$, the average northward displacement velocity is around $V_{eddy} \approx 6 \cdot 10^{-2}\text{ms}^{-1}$, while the fluid velocity in their interior reaches speed of $v_{eddy} \approx 2.4\text{ms}^{-1}$.

With the TW forcing the boundary layer is stabilized by the inertial effect as discussed in subsection 4.2 above. There are no eddies south of $y = +1000\text{km}$, the latitudes at which the time averaged zonal velocity is negative. At higher latitudes and for a viscosity of $\nu = 1000\text{m}^2\text{s}^{-1}$ a single eddy is created that migrates northward to the northwest corner of the domain, where it stabilizes. A chaotic eddy dynamics appears for the viscosities of $\nu = 500\text{m}^2\text{s}^{-1}$ and below at latitudes higher than $y = +1000\text{km}$. The eddies have an average tendency to migrate eastward and the fluid velocities reach locally up to $v_{eddy} \approx 2.4\text{ms}^{-1}$.

4.3.2 Bursts

For the lowest values of the viscosity, intermittent detachments of the viscous sub-layer just northward of the eddy center are observed at the boundary (see Fig.3). The viscous sub-layer is the thin layer of a few tens of kilometers thickness, for the lower viscosity values, at the boundary where the vorticity has large positive values. It is discussed in detail in subsection 4.6 of this section. The detachments are the most violent phenomena in the simulations (with viscosities $\nu = 500\text{m}^2\text{s}^{-1}$ and lower) with the strongest velocity and vorticity gradients. When the sheet of positive vorticity (the viscous sub-layer) along the western boundary in the Munk-layer breaks due to the action of an anticyclone, the south part of the viscous sub-layer detached, is torn of the boundary by the anticyclone and accelerates away from the boundary (see Fig.3). North of the detachment the vorticity anomaly and the meridional velocity are negative. The north part of the viscous sub-layer continues to flow northward along the boundary. These events are the analog to bursts or ejections in the classical boundary layer (Robinson (1991)) and are thus given the same name here. They are strong spatially localized and temporally intermittent ejections of fluid and vorticity away from the wall, initiated by the large anticyclonic eddies. The separation of the boundary layer plays a key role in boundary layer dynamic since Prandtl (1904), see also Schlichting and Gertsen (2000).

Experiments	TW125	TW150	TW250	TW300	TW400	TW500	TW1000
T1(%)	0.93	0.8	0	0	0	0	0
T2(%)	15.57	11.62	4.81	2.63	0.52	0	0
Experiments				MW300	MW400	MW500	MW1000
T1(%)				21.67	17.5	13.57	0
T2(%)				19.07	14.36	10.38	0

Table 2. Fraction of time with flow reversal in the viscous sub-layer where inertial effects are present at $y = +1000\mathrm{km}$ (T1); and for the whole WBC $y \in [+125, +2250\mathrm{km}]$ (T2).

The ejection of the boundary layer and its offshore transport, asks for fine resolution in both horizontal directions not only in the vicinity of the boundary layer but also in areas to which the boundary layer fragment is transported.

In our analysis we identify bursts as events when the meridional velocity in the viscous sub-layer is negative. Please note that the dynamics in the viscous sub-layer is not laminar, a feature that is also found in turbulent wall bounded flows in engineering applications (Robinson (1991)). To quantify the occurrence of burst, the fraction of time with flow reversal at $y = +1000\mathrm{km}$ is given by the T1 and the average over time and the interval $y \in [+125, +2250\mathrm{km}]$ by T2 in Tab.2. In the MW experiments the fraction of time with flow reversal is similar at $y = +1000\mathrm{km}$ than those of the range of latitude between $y \in [+125, +2250\mathrm{km}]$ meaning that there is only a feeble dependence on latitude. In the TW experiments almost no bursts occur south of $y = +1000\mathrm{km}$ in accord with the fact that there are no eddies south of $y = +1000\mathrm{km}$ in the TW experiments as mentioned above (subsection 4.3.1). For viscosities $\nu = 1000\mathrm{m}^2\mathrm{s}^{-1}$ or larger there are no bursts in both type of wind forcing. Bursts are observed for $\nu = 500\mathrm{m}^2\mathrm{s}^{-1}$ and lower in the MW experiments and for $\nu = 400\mathrm{m}^2\mathrm{s}^{-1}$ and lower in the TW experiments. The fraction of time with flow reversal strictly increases with decreasing viscosity in all the experiments performed and reaches values of around 20% for the lowest values of the viscosity, showing that they are a recurrent dominant feature of low viscosity boundary currents when inertial effects are absent.

4.3.3 Dipoles

In many instances the positive vorticity anomalies, ejected from the boundary during bursts, pair with negative vorticity anomalies from within the anticyclones and form dipoles (see Fig.3) which then travel ballisticaly (at almost constant velocity) over distances of several eddy diameters. The size of the dipoles measured by the distance of the vorticity minima and maxima spans between the thickness of the viscous boundary layer δ_ν (see below) and the size of the coherent anticyclones.

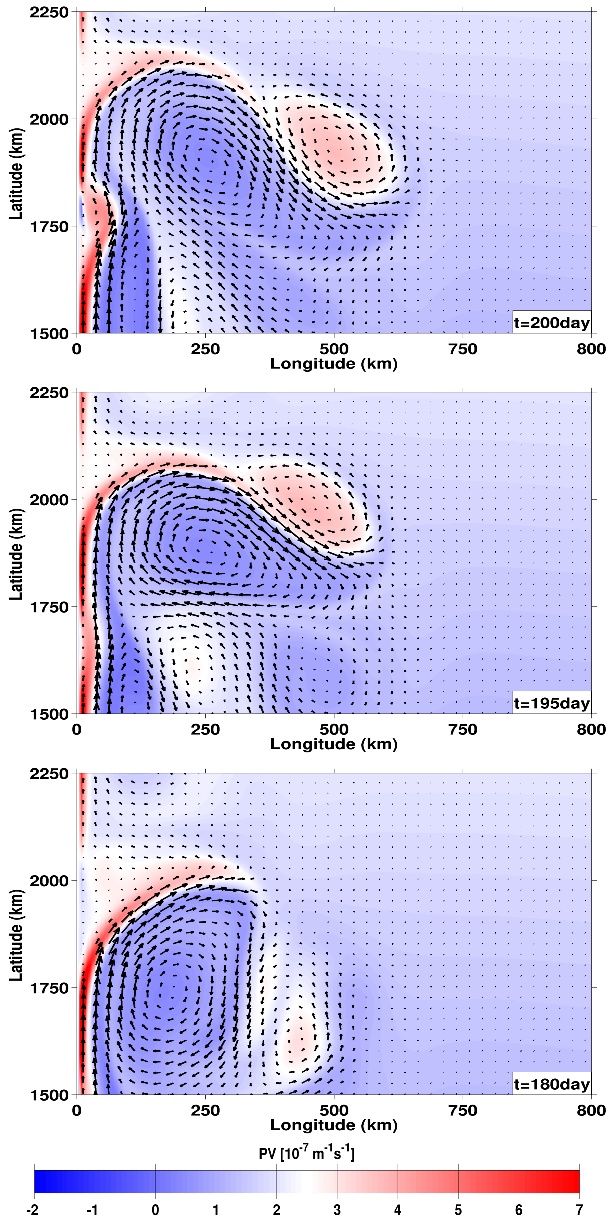

Fig. 3. Sequence of potential vorticity ($m^{-1}s^{-1}$) snapshots showing bursts and its subsequent development into a dipole for the lowest viscosity Monsoon Wind experiment (MW300). From bottom to the top, the snapshots were taken at t = 180, 195 and 200 days, .

4.4 Scales of motion

For an understanding of the dynamics it is essential to determine the spatial scales of the turbulent motion. We consider two key quantities. The first is twice the time averaged kinetic energy (per unit mass) divided by the time averaged enstrophy (square of vorticity):

$$\lambda_1 = \sqrt{\frac{\langle u^2 + v^2 \rangle}{\langle \zeta^2 \rangle}}. \tag{13}$$

These quantity is shown in Figs.4 and 5. In 3D turbulence it is the Taylor-scale divided by $\sqrt{5}$ (see Frisch (1995)). This length scale characterizes the size of the velocity gradients. The second length scale is the time averaged enstrophy divided by the time averaged palinstrophy (square of the vorticity gradient):

$$\lambda_2 = \sqrt{\frac{\langle \zeta^2 \rangle}{\langle (\nabla \zeta)^2 \rangle}}. \tag{14}$$

These quantity is shown in Fig.5. It is characteristic of the viscous dissipation length-scale in the enstrophy cascade (Bofetta and Ecke (2012)), the smallest scales in the vortical dynamics. The separation between the two scales gives an idea of the scale range over which turbulence is active. These scales are instructive in a turbulent environment but in the boundary layer dominated by viscosity their significance is limited. At the boundary $\lambda_1 = 0$ as energy vanishes, which does not mean that we have infinitely small scales there. At high viscosity the smallest scale is given by the Munk scale δ_{M} even when the analytic solutions for the laminar Munk-layer are (with $x' = \sqrt{3}x/(2\delta_{\mathrm{M}})$):

$$\lambda_1 = \delta_{\mathrm{M}} \sqrt{\left(\frac{2\sin(x')}{\sin(x') - \sqrt{3}\cos(x')} \right)^2} \text{ and } \lambda_2 = \delta_{\mathrm{M}} \sqrt{\left(\frac{\sin(x') - \sqrt{3}\cos(x')}{\sin(x') + \sqrt{3}\cos(x')} \right)^2}, \tag{15}$$

which oscillate between zero and infinity. This shows that the above scales are not useful for analyzing time-independent flow. Note, that traces of these oscillations remain in the low viscosity experiments, as can be seen in Figs.4 and 5.

Fig.4 shows the spatial distribution of the Taylor scale in the highest Reynolds number experiments for the MW and TW forcing, respectively. A striking feature is the wide extension of the low-size values into the interior of the domain in both cases, the feeble variation within this domain and the sudden jump to high values at its clearly defined boundary as seen in Figs.4 and 5. A clear plateau at around a scale of 60km is observed which extends of up to 2000km into the interior of the domain. We call the area of the plateau, the extended boundary layer (EBL). The scale of 60km is easily explained by the eddy size of $400\mathrm{km} \approx 2\pi 60\mathrm{km}$. Fig.5 shows that the width of the extended boundary layer is increasing with decreasing viscosity. The dissipation length scale λ_2 is smallest near the boundary and increases slowly there after, approaching the Taylor scale. When λ_2 reaches the eddy scale λ_1, the velocity gradients are dissipated and turbulence disappears. A sharp

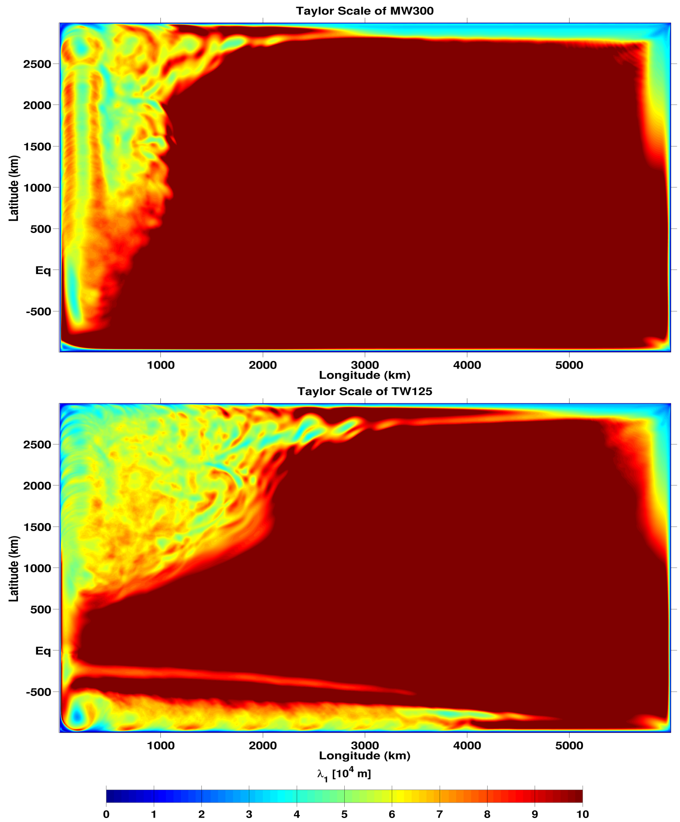

Fig. 4. Taylor scale λ_1 (Eq. (13)) for the lowest viscosity Monsoon Winds MW300 (above) and Trade Winds TW125 (below) experiments. Note that the colorbar stops at 100km to emphasize the behavior in the extended boundary layer (plateau of $\lambda_1 \sim 60$km).

boundary between turbulent areas and a laminar environment is observed in many instances when turbulence arises from a single process such as turbulent jets, planetary boundary layers, gravity currents and stratified turbulence. A sharp boundary between turbulent areas in a laminar environment is observed in many instances when turbulence arises from a single process such as turbulent jets, planetary boundary layers, gravity currents and stratified turbulence. The behavior of both scales, λ_1 being constant and λ_2 increasing by barely a factor of two through the extended boundary layer, shows that grid refinement near the boundary might be useful in laminar, low Reynolds number simulations, but is not adapted for the fully turbulent case where small scale structures dominate throughout the extended boundary layer. The zonal extension of the extended boundary layer increases with a decreasing viscosity as shown in Fig.8 and quantified in subsection 4.6. Supposing a scaling behavior for the extension of the extended boundary layer with viscosity in the MW forcing experiments suggests an exponent close to $-2/3$ as shown in Tab.3. An exponent that we can not explain. A striking feature is that, although the extension of the extended boundary layer depends on viscosity, the scales within it appear almost independent of it, once the viscosity is low enough to allow for turbulent motion. Turbulent motion in the extended boundary layer is likely to include the range of scales from λ_1 down to λ_2.

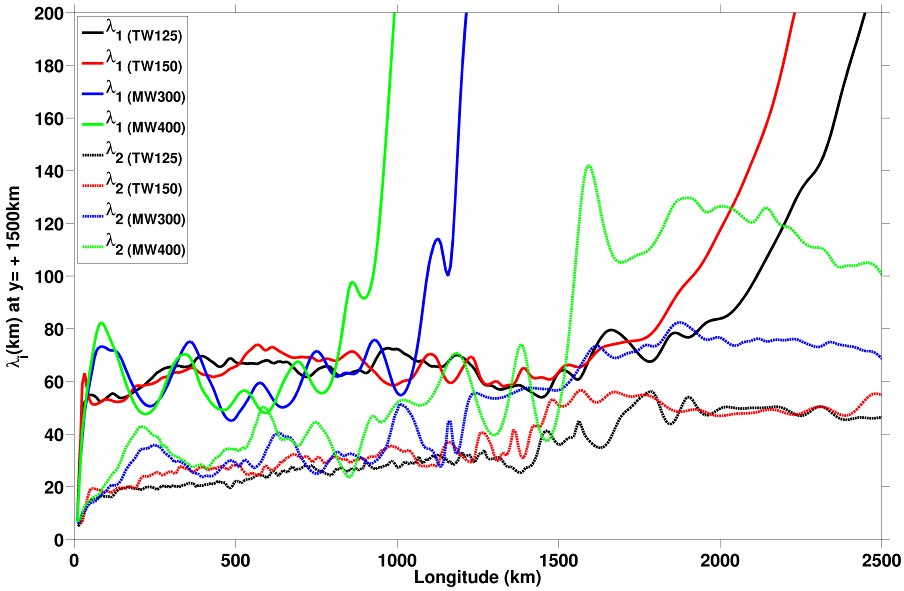

Fig. 5. Zoom of zonal profiles of the Taylor scale λ_1 (solid lines, Eq. (13)) and the viscous dissipation length-scale λ_2 (dashed lines, Eq. (14)) at latitude $y = +1500$km for the most turbulent experiments TW125, TW250, MW300 and MW400.

It is important to notice that in our calculations λ_2 is always more than 5 times the grid size showing that the dynamics is numerically well resolved in our calculations.

4.5 Moments of the velocity field

After having discussed the time averages of the velocity components, we will now focus on higher order moments of the fluctuations of these components. We suppose that the dynamics is in a statistically stationary state and we separate the variables into a time average and a perturbation that is: $a = \langle a \rangle + a'$. The higher order moments of the velocity components are given in Fig.6, where they are also compared to the moments of a disc of radius R in anticyclonic solid-body rotation. Taking the averages of moments of the velocity fluctuations in the y-direction over the disc, is equivalent to taking time averages at one y-location of a disc (or a succession of disks) transported by a mean flow in the y-direction at constant velocity. The comparison, presented in Fig.6, shows that major aspects of the turbulent fluxes can be, to a good accuracy, explained by the anticyclonic discs in solid-body rotation. This confirms, that the anticyclones are the dominant coherent structures.

The positive value of $\langle u'^3 \rangle$, however, can not be explained by the model of a disc moving in the meridional direction at constant speed, which leads to a vanishing third order moment. It is most likely a signature of the bursts and dipoles, with more intense and localized transport away from the

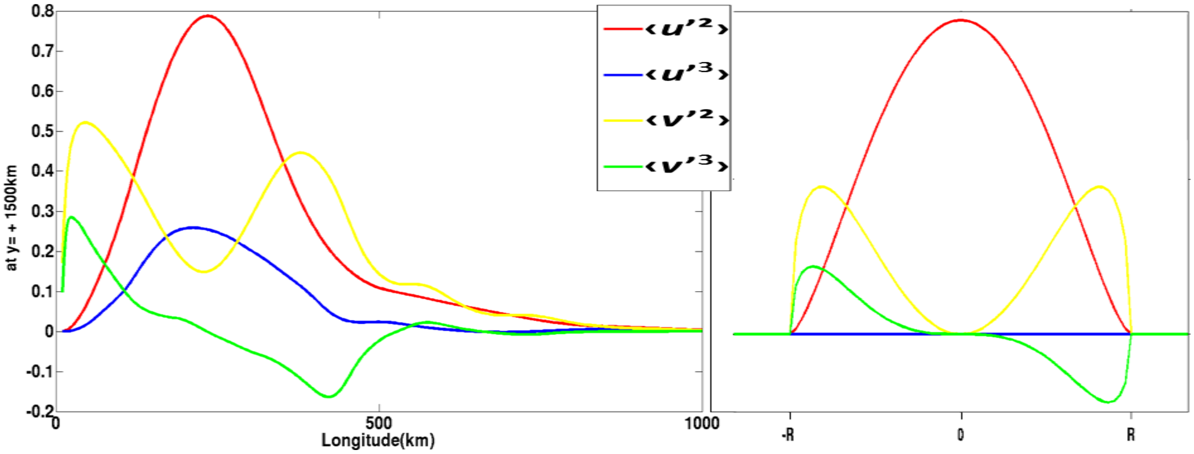

Fig. 6. Second and third order moments of the fluctuations of the velocity components from MW300 at $y = +1500$km as a function of the distance from the boundary (left). And the analytic solutions of the same quantities for a disc in anticyclonic solid-body rotation (right).

boundary than the recirculation towards the boundary. This agrees with the findings of anisotropic bursts and dipoles dynamics in subsection 4.3.

4.6 Vorticity Fluxes

The vorticity balance in the laminar, time independent, boundary layer is described in section 4.2. In the unstable boundary layer the vorticity balance changes. When time averaging is applied to Eq.(7) it transforms to:

$$\partial_x \left[\langle u\rangle\langle\xi\rangle\right] + \partial_y \left[\langle v\rangle\langle\xi\rangle\right] + \partial_x\langle u'\xi'\rangle + \partial_y\langle v'\xi'\rangle + \beta\langle v\rangle$$
$$+ f(\partial_x\langle u\rangle + \partial_y\langle v\rangle) - \nu\nabla^2\langle\xi\rangle = \langle F\rangle. \tag{16}$$

In a statistically stationary state a time average of an integration of the advection of vorticity over a closed basin vanishes and the integral balance is between the forcing (r.h.s of Eq.(16)) and the viscous vorticity flux through the boundary (last term on the l.h.s. of Eq.(16)). Within the basin the advection of vorticity can connect the (basin-wide) source to the sink. The different terms in the l.h.s of Eq.(16) correspond to the relative vorticity advection (RVA, terms 1 and 2), turbulent relative vorticity advection (TRVA, terms 3 and 4), planetary vorticity advection (PVA, term 5), stretching (STR, term 6) and friction (FRIC, term 7). The stretching term is negligible and does not contribute significantly to the vorticity the balance (see Fig.7). For high viscosities the local vorticity balance in the boundary layer is, to leading order, between the planetary vorticity advection (term 5) and the vorticity dissipation (term 7), leading to a Munk-layer as discussed in subsection 4.2 of this section. When the viscosity is reduced the relative vorticity advection term and its turbulent part

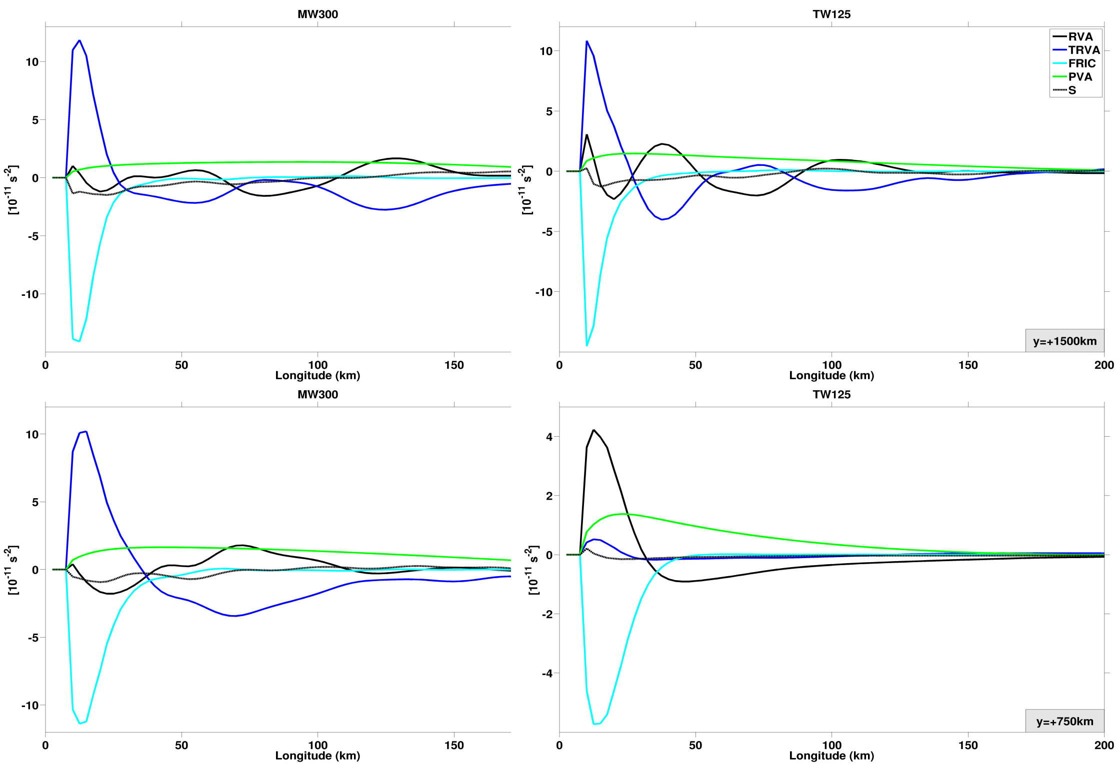

Fig. 7. Vorticity balance. Different terms of Eq.16 are plotted for the lowest viscosity experiments MW300 (right panels) and TW125 (left panels), at $y = +1500$km (top figures) and $y = +750$km (bottom figures). The different terms of Eq.(16) plotted correspond to the relative vorticity advection (RVA, terms 1 and 2), turbulent relative vorticity advection (TRVA, terms 3 and 4), planetary vorticity advection (PVA, term 5), friction (FRIC, term 7) and S comprises forcing, stretching and residual time dependence.

play an increasing role in the vorticity balance. The advection of relative vorticity spatially connects the transport of planetary vorticity and the viscous dissipation and both can exhibit a different zonal length scale. This is clearly visible in Fig.7: the friction dominates in a narrow region near the boundary, whereas the planetary vorticity advection extends further from the boundary. We call the area of the viscous dissipation the viscous sub-layer (VSL) while we choose the expression "advective boundary layer" (ABL) for the wider area of large average meridional velocity. The thickness of the former is denoted by δ_ν while the thickness of the latter is given by the symbol δ_A. In the Munk-layer theory they both coincide $\delta_\nu = \delta_A = \delta_M$. According to the shape of the different terms in Eq.(16) (shown in the Fig.7), we estimate the thickness of the viscous sub-layer by the distance from the boundary at which the absolute value of the Laplacian of the average vorticity has reduced to a third of its maximal value. The same criterion was applied to the average meridional velocity to obtain δ_A. Results for the corresponding boundary layer scales for the MW and TW cases and at different latitudes as a function of viscosity are assembled in Fig.8. For the viscous sub-layer results show that its thickness drops well below the Munk-scale for the lower viscosities, while the thickness of the advective boundary layer is always above. The advection of relative vorticity can be decomposed into the advection of the average vorticity by the average velocity field (RVA), which we call inertial contribution, and the turbulent transport of vorticity (TRVA). The difference between the TW and the MW circulation at low latitude is that, for the former the inertial terms are important while for the later the turbulent terms transport the vorticity. This explains the laminar boundary layer of the TW circulation at low latitude and the turbulence of the MW boundary layer. Please note that the inertial boundary layer in the TW circulation stays laminar even for the smallest viscosity used, if it becomes turbulent at even lower viscosities, is an open question. This behavior is clearly depicted in Fig.7, where at low latitudes of the TW circulation the inertial part connects the planetary vorticity advection to the viscous dissipation, whereas at higher latitudes and for the MW circulation it is the turbulent advection. Please note that Ierly and Young (1991) propose a scaling of $\delta_\nu \sim \nu^{1/6}$ for the boundary layer with an inertial component based on laminar boundary layer theory and an ansatz for the shape of the boundary layer. We analyzed the scalings of the turbulent boundary layer thickness by considering values obtained from turbulent boundary layers. Our results for the inertial boundary layer, see Tab.3, show a much steeper scaling of $1/2$ at low latitudes. This exponent suggests that the dominant vorticity advection near the boundary does not depend on the viscosity and has to be balanced at the boundary by viscous dissipation. At higher latitudes the scaling is higher for the TW forcing, showing that the boundary layer thickness decreases even faster with decreasing viscosity, when ”inverse inertial” effects are present, that is when the zonal velocity at the outer boundary of the boundary-layer is positive. In Fig.7 the inertial part shows an oscillatory behavior at high latitudes for the TW forcing, where the zonal velocity is positive, which leads to an inertial boundary layer scale that is complex valued, which explains the oscillations.

The scaling of the advective boundary layer thickness δ_A for the MW forcing shows a slight increase with decreasing viscosity (see Tab.3) and a possible saturation around 200km. For the TW forcing δ_A shows a slight decrease with decreasing viscosity at low latitude and a saturation at the value corresponding to the inertial boundary layer. At higher latitude, where an inverse inertial boundary layer is present, the thickness of the advective boundary layer still increases with decreasing viscosity.

4.7 Estimation of the eddy viscosity via the Munk formula

We have shown in section 4.2 and Fig.2 that the profile of the meridional velocity in the stationary boundary layer is close to the shape of the Munk-layer, when inertial effects are absent. When turbulence is present the shape of the time averaged meridional velocity still somehow resembles the Munk-layer solution with the meridional velocity vanishing at a distance x_0 from the boundary. For the Munk layer we have $x_0 = (2\pi/\sqrt{3})\delta_{\mathrm{M}}$. The meridional gradient in layer thickness (s) imposed by the large-scale circulation adds a topographic $\beta_{\mathrm{topo}} = -fs/H$ to the planetary value. Its value depends only weakly on the viscosity. When the effective β-term, composed of the planetary and

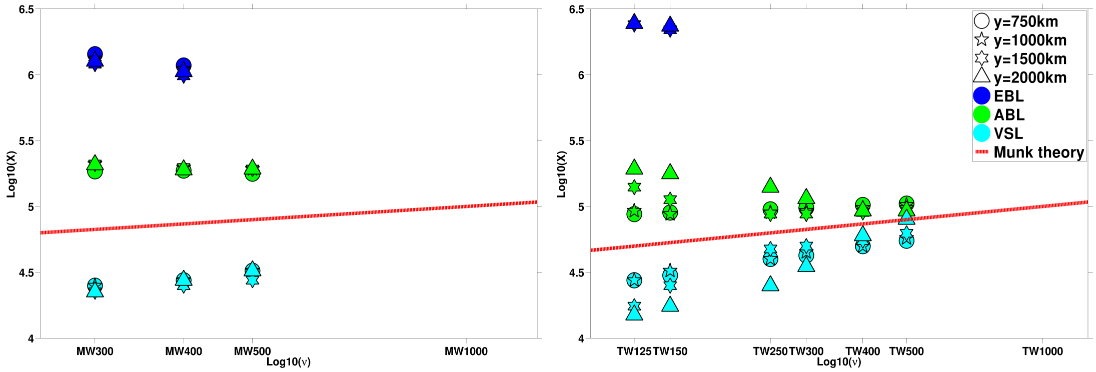

Fig. 8. Thickness of the viscous sub-layer (VSL), the advective boundary layer (ABL) and the extended boundary layer (EBL) for MW forcing (left) and TW forcing (right) experiments at different latitudes y.

	MW			TW		
y(km)	VSL	ABL	EBL	VSL	ABL	EBL
+750	0.50	-0.07	-0.68	0.50	0.13	–
+1000	0.50	-0.17	-0.63	0.50	0.08	–
+1500	0.39	-0.17	-0.71	0.89	-0.27	-0.48
+2000	0.71	-0.15	-0.62	1.20	-0.57	-0.25

Table 3. Scaling exponents of the zonal extension of the viscous sub-layer (VSL) thickness, the advective boundary layer (ABL) thickness and the extend boundary layer (EBL) thickness at different latitudes y for the MW forcing and the TW forcing.

topographic part, is constant, the Munk-layer scale is proportional to the cubic-root of the (eddy) viscosity and so is x_0. The idea is now to calculate an eddy viscosity ν_{eddy} based on x_0. To this end we measure the value x_0 in an experiment with high viscosity $\nu_{stat} = 1000\text{m}^2\text{s}^{-1}$ that has a time-independent dynamics and compare it to the value obtained from the average of a turbulent experiment at the same latitude. The eddy viscosity can then be obtained by using the proportionality:

$$\nu_{\text{eddy}} = \left(\frac{x_0}{x_0(\nu_{stat})}\right)^3 \nu_{\text{stat}}. \tag{17}$$

Such method can not be applied to the inertial boundary layer as, in this case the average meridional velocity decays exponentially away from the boundary and does not vanish. The following analysis was not applied to the inertial boundary layer. A clear scaling for $\nu'_{\text{eddy}} = \nu_{\text{eddy}} - \nu$ as a function of the zonal maximum of the r.m.s. velocity fluctuations $u'_{\text{r.m.s.}}$ is observed in Fig.9, for data from the MW and TW forcing at higher latitudes. The scatter plot is well fitted by an affine regression line of equation

$$\nu'_{\text{eddy}} = \nu_{\text{eddy}} - \nu = \cdot u'_{\text{r.m.s.}} \cdot 6283.3\text{m} - 639.3\frac{\text{m}^2}{s}, \tag{18}$$

which means that whatever the forcing and the viscosity, there is a correlation between the eddy viscosity and the fluctuating velocity. The correlation of the best fit linear regression is R = 0.97. The finding that for small values of $u'_{\mathrm{r.m.s.}}$ there is no turbulent contribution to the eddy viscosity is explained by the fact, that the small perturbations have a wave-like structure which do not lead to turbulent fluxes.

The simplest way to estimate a eddy viscosity proposed by Prandtl (1925) Mischungsweg (mixing length) λ and the fluctuating velocity $u'_{\mathrm{r.m.s.}}$ is:

$$\nu'_{\mathrm{eddy}} = \nu_{\mathrm{eddy}} - \nu = \alpha \lambda_1 u'_{\mathrm{r.m.s.}} \tag{19}$$

The results of the nonlinear experiments confirm this proportionality. For our data and $\lambda_1 = L_{\mathrm{eddy}}/(2\pi) = 60\mathrm{km}$ calculate previously we obtain $\alpha \approx 0.1$. If we suppose, that the eddy viscosity is due to the anticyclones this value of α is within the range proposed by Smagorinsky (1993). The values of λ_1 and $u'_{\mathrm{r.m.s.}}$ can not be obtained from external parameters but are a result from the numerical experiment. In concrete cases, they can often be obtained from observation or fine resolution numerical simulations.

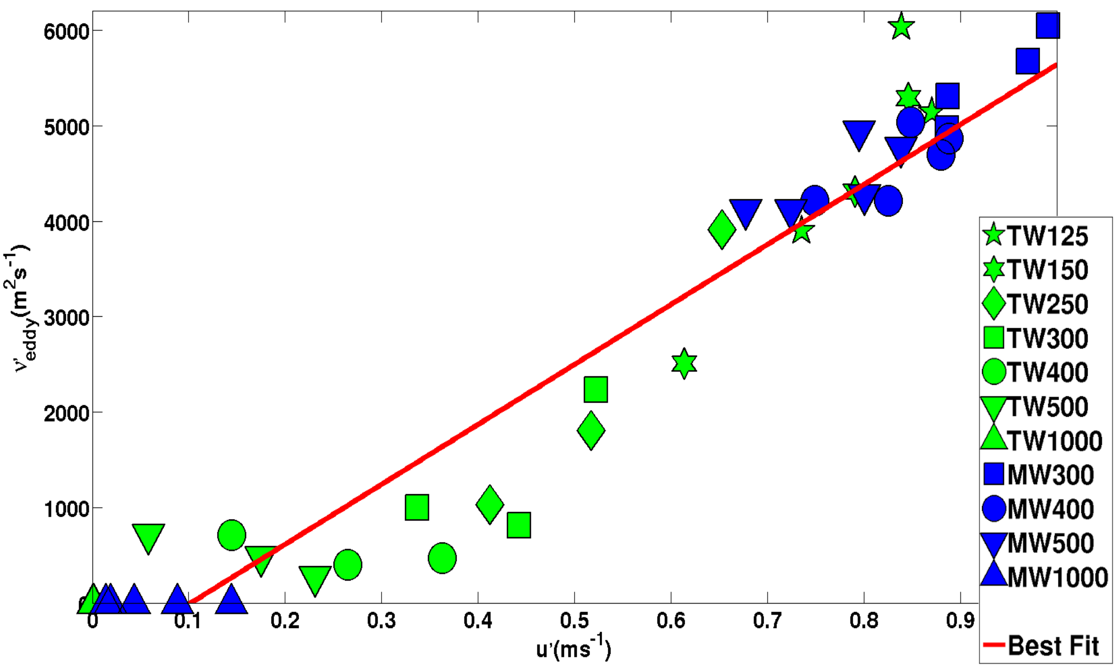

Fig. 9. Scatter plot diagram of eddy viscosity $\nu'_{\mathrm{eddy}} = \nu_{\mathrm{eddy}} - \nu$ computed from the data using the Munk formula approach of Eq.(17), as function of the maximum fluctuating velocity for all the nonlinear experiments at high latitudes $y = +1500$, $y = +1750$ and $y = +2000\mathrm{km}$. The green symbols represent the experiments with TW forcing and the blue ones those of MW forcing and the red line is the best fit affine regression line.

Using $\alpha = 0.1$ and the typical values for the Somali current of $L_{\mathrm{eddy}} = 400\mathrm{km}$ and $u'_{\mathrm{r.m.s.}} = 1\mathrm{ms}^{-1}$ leads to $\nu_{\mathrm{eddy}} \approx 6000\mathrm{m}^2\mathrm{s}^{-1}$ and a $\delta_{\mathrm{Munk}} \approx 70\mathrm{km}$. A consequence of this is that even a noneddy permitting ocean model should have a grid size not exceeding 50km to capture the boundary layer dynamics and the associated meridional heat transport at least in an average sense and no value of the eddy viscosity larger than $6000\mathrm{m}^2\mathrm{s}^{-1}$ should be used.

This pragmatic approach leads to a viscosity and a boundary layer thickness that compares well to average values in the turbulent boundary current. This approach is of course questionable as the eddy size is larger than the mean current, that is the scale separation is smaller than unity and the eddy viscosity approach asks for large scale-separations. This problematic was already noticed by Charney (1955) who states: "In order to account for the observed width of the current, Munk was forced to postulate an eddy viscosity so large that the eddy sizes were themselves comparable to the width"

We have estimated the eddy viscosity based on the average meridional velocity and have shown, that it can be connected via Prandtl's formula to the velocity fluctuations. This is however not a parameterization as the turbulent fluxes themselves are not obtained from the large-scale dynamics.

5 Discussion and Conclusions

In the MW forcing case the boundary current crosses the equator and we have not observed that the vanishing of the Coriolis parameter at the equator plays a special direct role in the dynamics of western boundary currents. In the TW forcing case the equatorial current splits up and flows poleward in both hemispheres as a western boundary current. In our calculations the importance of the equator is due to the larger latitudinal velocities (inertial effect) and the unstable wave dynamics at the equator, which increases the variability, also at the western boundary. To leading order, the vanishing of the Coriolis parameter is important due to its determination of the dynamics in the interior ocean, which then governs the boundary-layer structure. Without the stabilizing inertial effects, the transport of PV towards the boundary area, the western boundary layer does not exist as a continuous flow for high Reynolds number flow. The western boundary is a turbulent region with interacting eddies, bursts and dipoles and frequent velocity inversions. A laminar boundary layer structure can be recovered in an average sense. The turbulent dynamics leads to a split up of the boundary layer into three layers: a viscous sub-layer, an advective boundary layer and an extended boundary layer. The thickness of the viscous sub-layer (VSL) increases with viscosity, that of the extended region (EBL) decreases and the advective region (ABL) stays essentially unchanged, once it drops below values that allow for turbulent motion.

We identified for the lower values of the viscosity a sequence in the evolution of the dynamics of the coherent structures: anticyclones are generated by instability, during their northward migration they intermittently detach parts of the viscous sub-layer containing strong positive vorticity, these bursts pair with negative vorticity from within the anticyclones and form dipoles which then travel ballisticaly (at almost constant velocity) over distances of several eddy diameters. In observations (called ”flanking cyclones” by Beal and Donohue (2013)) and a fine resolution Ocean General Circulation Models (Akuetevi et al. (in prep.)) bursts are seen to lead to substantial upwelling of cold and nutrient rich water-masses from the deep. The dipole transports these water-masses offshore, leading to an increased biological production several hundreds of kilometers from the coast (Kawamiya and Oschlies (2003); Wirth et al. (2001)). The above is an example of how meso and sub-meso scale activity can increase biological activity.

We showed that the turbulent eddy dynamics is the natural state of the high Reynolds number low latitude western boundary current. In this perspective, the question is not why eddies are present, but to the contrary, how inertial effects allow for the existence of a coherent western boundary current. When a flat boundary is used, the thickness of the viscous sub-layer goes to zero with viscosity.

5.1 Conclusions concerning numerical simulation of turbulent boundary layers

It is the thickness of the viscous sub-layer that imposes the spatial resolution of a numerical model. The thickness of the turbulent viscous sub-layer decreases faster with decreasing viscosity than the prominent $\frac{1}{3}$ scaling from Munk-layer theory, in all our experiments performed and at all latitudes considered. The laminar Munk-layer theory is however used to determine the (hyper) viscosity for a given spatial resolution in todays simulations of the ocean dynamics. The here presented results prove, that for the turbulent boundary layer, the choice of spatial resolution based on the Munk-layer theory is far from being sufficient. For the same viscosity, the viscous sub-layer of the MW forcing experiments is thinner than in TW forcing experiments (see Fig.8), which explains why the experiments of the MW forcing were only possible down to $\nu = 300\mathrm{m}^2\mathrm{s}^{-1}$ while the experiments with the TW forcing converged down to $\nu = 125\mathrm{m}^2\mathrm{s}^{-1}$.

From Fig.8 it is clear that the difference between the thickness of the extended boundary layer and the viscous sub-layer widens with increasing Reynolds number. The difference is a measure of the complexity of the numerical calculations of low latitude turbulent WBCs as the finest scale δ_ν has to be resolved throughout δ_{ext} in both horizontal directions. This shows that grid refinement near the boundary, that is using a finer grid closer to the boundary than further away, has no place in simulations of the turbulent boundary layer as: (i) the structures are almost isotropic and (ii) the small scales extend far from the boundary.

The extension of the extended boundary-layer, the area over which turbulence is present, grows with decreasing viscosity whereas the size of the structures decreases. Therefore, higher viscosity runs require a higher resolution over a larger domain, increasing the complexity of the calculation.

5.2 Conclusions concerning the parameterization of the turbulent boundary layers

One of the major challenges in the numerical simulation of the ocean dynamics is to parameterize the effect of the small scale dynamics not explicitly resolved on the explicitly resolved large-scale flow.

Inertial theory and the above presented results teach us that small westward velocities can stabilize the western boundary layer. Velocity components in other directions have no such effect. A parameterization of the turbulence must therefore reflect this anisotropy. The instability of the boundary layer is also strongly dependent on details of the zonal velocity profile as noted by Ierly and Young (1991). Topographic features are also likely to play an important role in the stability and turbulent fluxes.

Our determination of the eddy viscosity in section 4.7 via the Munk formula is a parameterization as we related eddy viscosity to the maximum fluctuating velocity. These show that for the lowest viscosities, δ_A saturates at a value corresponding to $\nu \approx 6000\mathrm{m}^2\mathrm{s}^{-1}$. Choosing viscosity values lower than $\nu \approx 6000\mathrm{m}^2\mathrm{s}^{-1}$ but above the threshold for fully turbulent boundary layers $\nu \approx 300\mathrm{m}^2\mathrm{s}^{-1}$ leads to an unreal thin average boundary layer thickness, worsening of the representation of the advective boundary layer dynamics. In numerical simulations of the boundary layer dynamics one should either simulate the turbulent dynamics or parameterize it. In other words, our findings discussed above suggest that, one can either use fine resolution and a low viscosity ($\nu <\approx 300\mathrm{m}^2\mathrm{s}^{-1}$) to simulate the turbulent boundary or, one can use coarse resolution and a high viscosity ($\nu \approx 6000\mathrm{m}^2\mathrm{s}^{-1}$) and recover the time-averaged boundary layer dynamics. Using viscosities in the interval $300\mathrm{m}^2\mathrm{s}^{-1} < \nu < 6000\mathrm{m}^2\mathrm{s}^{-1}$ leads to a wrong time-averaged boundary-layer dynamics.

In our simulations we varied the eddy-viscosity parameter by roughly an order of magnitude. The corresponding necessary spatial resolutions vary from those of todays coarse resolution climate models down to those of fine resolution regional models. Our calculations suggest, that even lower viscosity values lead to smaller boundary layer scales and higher velocities. At smaller scales the hydrostatic approximation, on which the shallow water equations are based is no longer valid as the dynamics becomes truly three-dimensional. Higher velocities lead to Froude numbers exceeding unity, that is the fluid velocity is higher than the speed of the gravity waves. In this case, hydraulic jumps occur and the flow becomes fully three dimensional such phenomena can not be explicitly resolved by the two-dimensional shallow water equations. In Fox-Kemper and Pedlosky (2004) and Fox-Kemper (2004) this problems are bypassed by using a constant depth model, where Froude number vanishes and by increasing the viscosity in the vicinity of the boundary. We propose here a numerical value, based on the Prandtl formula, for the eddy viscosity in the vicinity of the boundary that leads to a laminar boundary layer mimicking (on average) the dynamics of turbulent boundary layers at lower viscosity.

We did not consider the more involved behavior of hyper dissipation operators (hyper-viscosity, powers of the Laplacian), which ask for boundary conditions for derivatives of the velocity field and which lead towards thermalization at small scales of the turbulent dynamics as explained by Frisch et al. (2008).

Acknowledgements.

References

Akuetevi, C. Q. C., Barnier, B., Molines, J.-M., and Lecointre, A.: Interactions between the Somali Current Eddies during the Summer Monsoon: Insights from a numerical study, preprint for Ocean Science, in prep.

Aubry, N., Holmes, P., Lumley, J. L., and Stone, E.: The dynamics of coherent structures in the wall region of a turbulent boundary layer, Journal of Fluid Mechanics, 192, 115–173, 1988.

Barnier, B., Reynaud, T., Beckmann, A., Böning, C., Molines, J.-M., Barnard, S., and Jia, Y.: On the seasonal variability and eddies in the North Brazil Current: insights from model intercomparison experiments, Progress in Oceanography, 48, 195–230, 2001.

Beal, L. and Donohue, K.: The Great Whirl: Observations of its seasonal development and interannual variability, Journal of Geophysical Research: Oceans, 2013.

Beal, L., Hormann, V., Lumpkin, R., and Foltz, G.: The Response of the Surface Circulation of the Arabian Sea to Monsoonal Forcing, Journal of Physical Oceanography, 43, 2008–2022, 2013.

Bofetta, G. and Ecke, R.: Two-Dimensional Turbulence, Annu. Rev. Fluid Mech., 44, 427–451, 2012.

Charney, J.: The Gulf stream as an inertial boundary layer, Proc Natl Acad Sci USA, 41, 731–740, 1955.

Cox, M. D.: A numerical study of Somali Current eddies, Journal of Physical Oceanography, 9, 311–326, 1979.

Edwards, C. A. and Pedlosky, J.: Dynamics of nonlinear cross-equatorial flow. Part 1: The tropically enhanced instability of the western boundary current., J. Phys. Oceanogr., 28, 2382–2406, 1998a.

Edwards, C. A. and Pedlosky, J.: Dynamics of nonlinear cross-equatorial flow. Part 2: The tropically enhanced instability of the western boundary current., J. Phys. Oceanogr., 28, 2407–2417, 1998b.

Fofonoff, N.: Steady flow in a frictionless homogeneous ocean, J. mar. Res, 13, 254–262, 1954.

Fox-Kemper, B.: Wind-driven barotropic gyre II: Effects of eddy and low interior viscosity, J. Mar. Res., 62, 195–232, 2004.

Fox-Kemper, B.: Reevaluting the roles of eddies in multiple barotropic wind-driven gyres, J. Phys. Oceanogr., 35, 1263–1278, 2005.

Fox-Kemper, B. and Pedlosky, J.: Wind-driven barotropic gyre I: Circulation control by eddy vorticity fluxes to an enhanced removal region, J. Mar. Res., 62, 169–193, 2004.

Fratantoni, D. M. and Richardson, P. L.: The Evolution and Demise of North Brazil Current Rings., Journal of physical oceanography, 36, 2006.

Fratantoni, D. M., Johns, W. E., and Townsend, T. L.: Rings of the North Brazil Current: Their structure and behavior inferred from observations and a numerical simulation, Journal of Geophysical Research: Oceans (1978–2012), 100, 10 633–10 654, 1995.

Frisch, U.: Turbulence: the legacy of A.N. Kolmogorov, Cambridge University Press, 1995.

Frisch, U., Kurien, S., Pandit, R., Pauls, W., Ray, S., Wirth, A., and Zhu., J.-Z.: Hyperviscosity, Galerkin Truncation, and Bottelnecks in Turbulence, Phys. Rev. Lett., 101, 144 501, 2008.

Garraffo, Z. D., Johns, W. E., P Chassignet, E., and Goni, G. J.: North Brazil Current rings and transport of southern waters in a high resolution numerical simulation of the North Atlantic, Elsevier Oceanography Series, 68, 375–409, 2003.

Garzoli, S. L., Ffield, A., and Yao, Q.: North Brazil Current rings and the variability in the latitude of retroflection, Elsevier Oceanography Series, 68, 357–373, 2003.

Ierly, G. R. and Young, W. R.: Viscous instabilities in the western boundary layer, J. Phys. Oceanogr., 21, 1323–1332, 1991.

Jiang, S., Jin, F.-F., and Ghil, M.: Multiple equilibria, periodic, and aperiodic solutions in a wind-driven, double-gyre, shallow-water model, Journal of physical oceanography, 25, 764–786, 1995.

Kawamiya, M. and Oschlies, A.: An eddy-permitting, coupled ecosystem-circulation model of the Arabian Sea: comparison with observations., J. of Marine Syst., 38, 221–257, 2003.

Lin, L. and Hurlburt, H.: Maximum simplification of nonlinear Somali Current dynamics, Monsoon dynamics, pp. 541–555, 1981.

McCreary, J. P. and Kundu, P. K.: A numerical investigation of the Somali Current during the Southwest Monsoon, Journal of marine research, 46, 25–58, 1988.

Munk, W. H.: On the wind-driven ocean circulation, J. Meteor., 7, 79–93, 1950.

Pedlosky, J.: Geophysical fluid dynamics, Springer Verlag, New York, http://opac.inria.fr/record=b1085573, includes index, 1979.

Pedlosky, J.: Geophysical Fluid Dynamics (2nd edition), Springer, iSBN-13: 978-0387963877, 1990.

Philander, S. and Delecluse, P.: Coastal currents in low latitudes (with application to the Somali and El Nino currents), Deep Sea Research Part A. Oceanographic Research Papers, 30, 887–902, 1983.

Philander, S. and Pacanowski, R.: The oceanic response to cross-equatorial winds (with application to coastal upwelling in low latitudes), Tellus, 33, 201–210, 1981.

Prandtl, L.: Uber Flussigkeitsbewegung bei sehr Keiner Reibung, Reprinted in Coll. Works, II, 575–584, 1904.

Prandtl, L.: Z. angew, Math. Mech., 5, (1)136–139, 1925.

Richardson, P. L. and Schmitz, W. J.: Deep cross-equatorial flow in the Atlantic measured with SOFAR floats, J. Geophys. Res., 98, 8371–8387, 1993.

Richardson, P. L., Hufford, G. E., Limeburner, R., and Brown, W.: North Brazil current retroflection eddies, J. Geophys. Res., 99, 5081–5093, 1994.

Robinson, S. K.: Coherent Motions in the Turbulent Boundary Layer, Ann. Rev of Fluid Mech., 23, 601–63, dOI: 10.1146/annurev.fl.23.010191.003125, 1991.

Schlichting, H. and Gertsen, K.: Boundary-Layer Theory, Springer Verlag, iSBN-13: 978-3540662709, 2000.

Schott, F. and McCreary, J.: The monsoon circulation of the Indian Ocean, Progress in Oceanography, 51, 1–123, 2001.

Schott, F. A., Xie, S.-P., and McCreary, J. P.: Indian Ocean circulation and climate variability, Reviews of Geophysics, 47, 2009.

Smagorinsky, J.: Some historical remarks on the use of nonlinear viscosities, In 'Large Eddy Simulation of Complex Engineering and geophysical Flows', Cambridge University Press, editors: B. Galperin an St. A. Orszag, 3–36, 1993.

Speich, S., Dijkstra, H., and Ghil, M.: Successive bifurcations in a shallow-water model applied to the wind-driven ocean circulation, Nonlinear Processes in Geophysics, 2, 241–268, 1995.

Stommel, H.: The westward intensification of wind-driven ocean currents, Trans. Amer. Geophys. Union, 29, 202–206, 1948.

Stommel, H.: Why do our ideas about the ocean circulation have such a peculiarly dream-like quality? Or examples of types of observations that are badly needed to test oceanographic theories, Collected Works of Henry M. Stommel, 1, 124–34, 1995.

Sushama, L., Ghil, M., and Ide, K.: Spatio-temporal variability in a mid-latitude ocean basin subject to periodic wind forcing, Atmosphere-Ocean, 45, 227–250, 2007.

Sverdrup, H. U.: Wind-driven currents in a baroclinic ocean; with application to the equatorial currents of the eastern Pacific, Proceedings of the National Academy of Sciences of the United States of America, 33, 318, 1947.

Vallis, G.: Atmospheric and Oceanic Fluid Dynamics, Cambridge Univ. Press., iSBN: 0-521-84969-1, 2006.

Van Heijst, G. and Flor, J.: Laboratory experiments on dipole structures in a stratified fluid, Elsevier oceanography series, 50, 591–608, 1989.

Wirth, A.: Inertia–gravity waves generated by near balanced flow in 2-layer shallow water turbulence on the β-plane., Nonlinear Processes in Geophysics, 20, 2013.

Wirth, A., Willebrand, J., and Schott, F.: Variability of the Great Whirl from observations and models, Deep-Sea Resea., II 49, 1279–1295, 2001.

Wirth, A., Willebrand, J., and Schott, F.: Variability of the Great Whirl from observations and models, Deep Sea Research Part II: Topical Studies in Oceanography, 49, 1279–1295, 2002.